Progress In Electromagnetics Research B, Vol. 81, 1–23, 2018

Wideband Radio Frequency Noiselet Waveforms for Multiresolution Nondestructive Testing of Multilayered Structures

Tae Hee Kim and Ram M. Narayanan*

Abstract—Developed initially for military applications, radar technology is rapidly spreading to areas as diverse as natural resource monitoring, civil infrastructure assessment, and homeland security. Waveform design is a critical component to extract maximum information about the targets or features being probed. Waveforms derived from noiselets, one of the family functions of wavelets, can be advantageous in certain applications owing to their random and uncorrelated properties. In this work, radio frequency (RF) noiselet waveforms are introduced and their performance related to detection of arbitrary target interfaces using the cross-correlation method, a form of matched filtering, is assessed. The application of the RF noiselet waveform for nondestructive testing (NDT) of the multilayered dielectric structures is discussed. The application of wideband noiselet waveforms for multiresolution analysis (MRA) is demonstrated.

1. INTRODUCTION

Radio frequency (RF) noiselets are herewith defined as short duration pulsed waveforms containing high frequency random signals within the pulse envelope. In other words, they can be considered as frequency modulated random waveforms. A noiselet originates from the definition of wavelets and has desirable properties for radar applications, such as mutual orthogonality, a flat Fourier transform, and the potential for multiresolution analysis (MRA) [1]. The noiselet has the structure of a sparse representation and it is composed of random noise coefficients. While the noiselet can be thought of as a pulsed wavelet, it is perfectly uncorrelated to the signal representation of wavelets. Thus, it is conjectured that noiselets could have the potential of higher probability of signal detection and recovery from sparse data [1, 2].

In any radar application, good range resolution is desired to better resolve closely spaced targets and features. For frequency modulated waveforms employing matched filtering, the range resolution ΔR is inversely proportional to the bandwidth B and is given by $\Delta R = c/2B\sqrt{\varepsilon}_r$, where c is the speed of light and ε_r is the dielectric constant of the medium [3]. A noise radar transmits a random signal and matched filtering is accomplished by cross-correlating the received signal with a time-delayed transmit signal replica. A noise radar system possesses low probability of interception (LPI), low probability of detection (LPD), and interference and jamming suppression, which are advantageous in RF-congested and RF-contested environments [4]. While a continuous wave (CW) wideband noise radar can achieve excellent range resolution based on the bandwidth, pulsed noise radars are preferred to eliminate problems associated with transmit-receive isolation and to reduce computational complexity [5]. By randomizing the signal from pulse to pulse, completely independent information is acquired from the target from each pulse [6].

Although ultrawideband (UWB) signals result in fine range resolution, feature information within multilayered structures can be better characterized by exploring the spatial neighborhood around the

Received 30 March 2018, Accepted 28 May 2018, Scheduled 4 June 2018
* Corresponding author: Ram M. Narayanan (ram@engr.psu.edu).
The authors are with the Department of Electrical Engineering, The Pennsylvania State University, University Park, PA 16802, USA.

nominal detection range. This can be implemented by collecting UWB data, processing the returns over the entire bandwidth (best resolution) and also over fractions of the bandwidth (progressively degraded resolutions), and using the combined information to assess the features being probed. The wavelet transform (WT) utilizes multiscale basis functions provide MR capability by processing radar echoes from both small-scale natural resonances as well as large-scale scattering center information [7].

2. WAVELET BASED RADAR

Wavelets are useful in analyzing patterns and features according to scale and wavelet algorithms process data at different scales or resolutions [8]. Gross features of a pattern are seen when it is observed through a large window, while smaller features are seen when observed through a small window. They are especially suited for approximating data with sharp discontinuities. A wavelet prototype function, called an analyzing wavelet or mother wavelet, is adopted for wavelet analysis. The WT is exploited in the analysis of nonstationary signals as an alternative to the classical short-time Fourier transform (STFT). The WT uses short windows at high frequencies and long windows at low frequencies in comparison to the STFT which uses a constant window [9].

In wavelet analyses, general functions are represented in terms of simpler, fixed building blocks at different scales and positions [10]. Various constructions of wavelets, such as orthogonal, semiorthogonal, and biorthogonal wavelets, are used in MRA. MR decompositions permit the scale-invariant interpretation of an image [11]. At coarse resolution, image details correspond to the larger structures which provide the image context. As resolution is gradually enhanced, finer structures begin to emerge. The selection of a proper mother wavelet is necessary for extracting the dynamic features of patterns for multiresolution analysis [12]. Noiselets have also been shown to serve as excellent tools for MRA, based on their extremely wide bandwidths [13].

Since a wavelet is a small oscillatory wave existing over a short duration with finite energy, it has an amplitude quickly decaying to zero in both the positive and negative directions. This makes wavelets suitable in electromagnetic (EM) analyses, such as EM scattering from sharp edges [14] and radar reflections from targets containing scatterers at different scales [15].

The concept of a wavelet-based radar was first introduced in [16] wherein the transmitted radar waveform was encoded with coefficients corresponding to a WT. Reflected radar waveforms were decoded using an inverse WT to produce a high range resolution profile of the target. A software defined radar wherein a wavelet signal was generated by an arbitrary waveform generator and upconverted to RF was tested successfully [17]. Wavelet-based radar waveforms have been investigated for several applications, including adaptive radar [18], range sidelobe suppression [19], detection of moving targets [20], synthetic aperture radar [21], and simultaneous high resolution in range and velocity [22]. In sonar, reverberations have been simulated using noiselets formed by sums of randomly weighted and delayed copies of the original transmit pulse [23].

3. RF NOISELETS GENERATION AND PROCESSING

3.1. Noiselet Generation

We generate RF noiselets by passing the output of a suitable noise source through a bandpass filter, which generates the appropriate waveform over the selected time span. The bandpass filter permits the adjustment of the frequency bandwidth of the UWB signals to achieve the desired range resolution. In our simulations, the bandwidth wasset to 4 GHz, which yielded a range resolution of 3.75 cm in air and 2.37 cm in a fiber reinforced plastic (FRP) material of a typical dielectric constant value of 2.5.

One simple design for the filter of noiselets is one with a rectangular power spectral density (PSD) envelope which is based on the Wiener-Khintchine theorem. In this paper, the filter design is based on fractions of the Nyquist sampling rate or frequency to achieve 4-GHz bandwidth. Fig. 1 shows a simplified block diagram for generating suitable noiselets from noise source. Depending on the original noise source, various noiselets can be created, such as random Gaussian, random binary, and random sinusoidal noiselets. However, a random sinusoidal noiselet, which was originally considered, is not discussed in this work due to the lack of random properties in either the time- or the frequency-domain.

The output of the bandpass filter, $X_{\text{noiselet}}(\omega)$ in the frequency domain, can be expressed as

$$X_{\text{noiselet}}(\omega) = H_{\text{bandpass}}(\omega) \cdot X_{\text{noise}}(\omega) \tag{1}$$

where $X_{\text{noise}}(\omega)$ is the output of the noise source, and $H_{\text{bandpass}}(\omega)$ is the frequency domain transfer function of the bandpass filter.

A random Gaussian noiselet is produced by a random number algorithm called the Mersenne twister (MT) [24]. The Mersenne twister achieves generation of very high-quality pseudorandom numbers with a long period length, and thus its output is free of long-term correlations. In addition, it passes several

Figure 1. Block diagram of bandpass filtering operation for noiselet generation from noise source (random coefficients) existing over the entire frequency band.

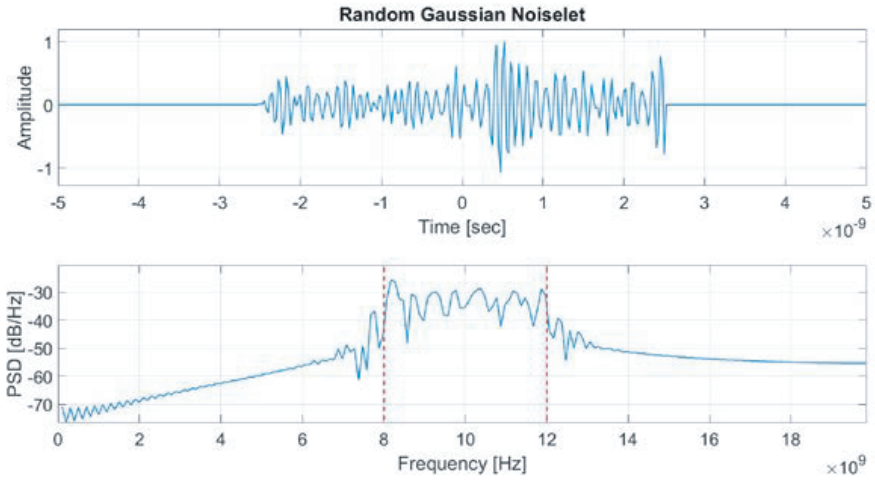

Figure 2. Amplitude (top) and spectral content (bottom) of (a) random Gaussian noiselet, and (b) random binary noiselet. The duration of each noiselet is 5 ns and its frequency range is 8–12 GHz.

tests for randomness. The Gaussian noiselet can be considered as Gaussian noise since the entire random signal is based on a Gaussian distribution such that the expectation value for random numbers from the noiselet generation will converge to that of the Gaussian distribution. The coefficients of random Gaussian noiselets can be achieved using following operation

$$\mathbf{x}_{k+n} := \mathbf{x}_{k+m} \oplus \left(\mathbf{x}_k^u | \mathbf{x}_{k+1}^l\right) \mathbf{A} \text{ for } k = 0, 1, \ldots \tag{2}$$

where $\mathbf{A}$ is a matrix with identity and word vectors; $\mathbf{x}$ stands for w-bit words; $\mathbf{x}_k^u$ represents the upper $(w - r)$ bits on $\mathbf{x}_k$; $\mathbf{x}_{k+1}^l$ represents the lower r bits on $\mathbf{x}_{k+1}$; $\oplus$ is the XOR operator; $|$ is the OR operator. The coefficients using the MT approach are computed for random numbers between -1 and $+1$.

Similar to the random Gaussian noiselet, a random binary noiselet is also based on the random Gaussian coefficients; however, it takes only the polarity of random coefficients from the random Gaussian noiselet. For example, positive coefficients will converge to '+1' compared to negative coefficients will automatically possess '−1'. Therefore, the random binary noiselet will fluctuate between '−1' and '+1'.

Figure 2 shows sample noiselets created based on previous descriptions at time- and frequency-domains depicting both the amplitude and the power spectral density (PSD). Since the signal is generated randomly each time, each realization is uncorrelated to another. The Gaussian wavelet shows a flatter response within the 8–12 GHz passband with good roll-off in the stopband, while the binary noiselet has significant variations within the passband and significant bleeding in the stopband. Therefore, averaging of multiple realizations is required to maintain smooth out the responses within the passband and to ensure a smooth roll-off in the stopband.

3.2. Noiselet Processing

Target or feature detection is accomplished by performing the matched filter operation, i.e., cross-correlation of the transmitted waveform with the received reflected waveform. Appropriate signal attenuation and time delays are introduced in the received waveform based upon the dielectric properties of the media through which the signal passes. Also, additive uncorrelated noise signals to the received waveform to simulate realistic field situations. After the matched filtering operation is performed, the highest peak locations yield the range to the target or feature of interest.

Let $x_t(t)$ represent the transmit signal and $x_r(t) = ax_t(t - t_0)$ represent the reflected signal from a target with a round trip time delay t_0, where a is the signal attenuation factor ($0 \leq a \leq 1$). The corresponding Fourier transforms are denoted by $X_t(\omega)$ and $X_r(\omega)$, respectively. Matched filtering is performed in the frequency domain by multiplying the two Fourier transforms and then taking the inverse Fourier transform (IFT) to return to the time domain. Thus, the matched filter output Fourier transform, $X_{mf}(\omega)$, is given by

$$X_{mf}(\omega) = X_t(\omega) \cdot X_r(\omega) \tag{3}$$

and its time domain representation is $x_{mf}(t) = \text{IFT}\{X_{mf}(\omega)\}$. The location of the peak of the matched filter response provides the range to the target.

Figure 3 shows a comparison in performance between the random Gaussian noiselet and a traditional wavelet used frequently, namely the Ricker or the Mexican hat wavelet. This wavelet is defined as the negative normalized second derivative of a Gaussian function, and is given by

$$x(t) = \frac{2}{\sqrt{3\sigma}\pi^{1/4}} \left(1 - \left(\frac{t}{\sigma}\right)^2\right) e^{-\frac{t^2}{2\sigma^2}} \tag{4}$$

where σ is a parameter which determines the temporal width of this wavelet. Both wavelets have the same time duration of 5 ns for meaningful comparison. We assume that multiple targets are located at distances of 30, 52.5, 90 cm, corresponding to round trip times of 2, 3.5, and 6 ns, respectively. Noise was added to the received signal to achieve a signal-to-noise ratio (SNR) of 20 dB. As can be noted, the noiselet achieves a more reliable determination of the target range, despite its random-like character, compared to the Mexican hat wavelet. In addition, it provides much better range resolution. It may

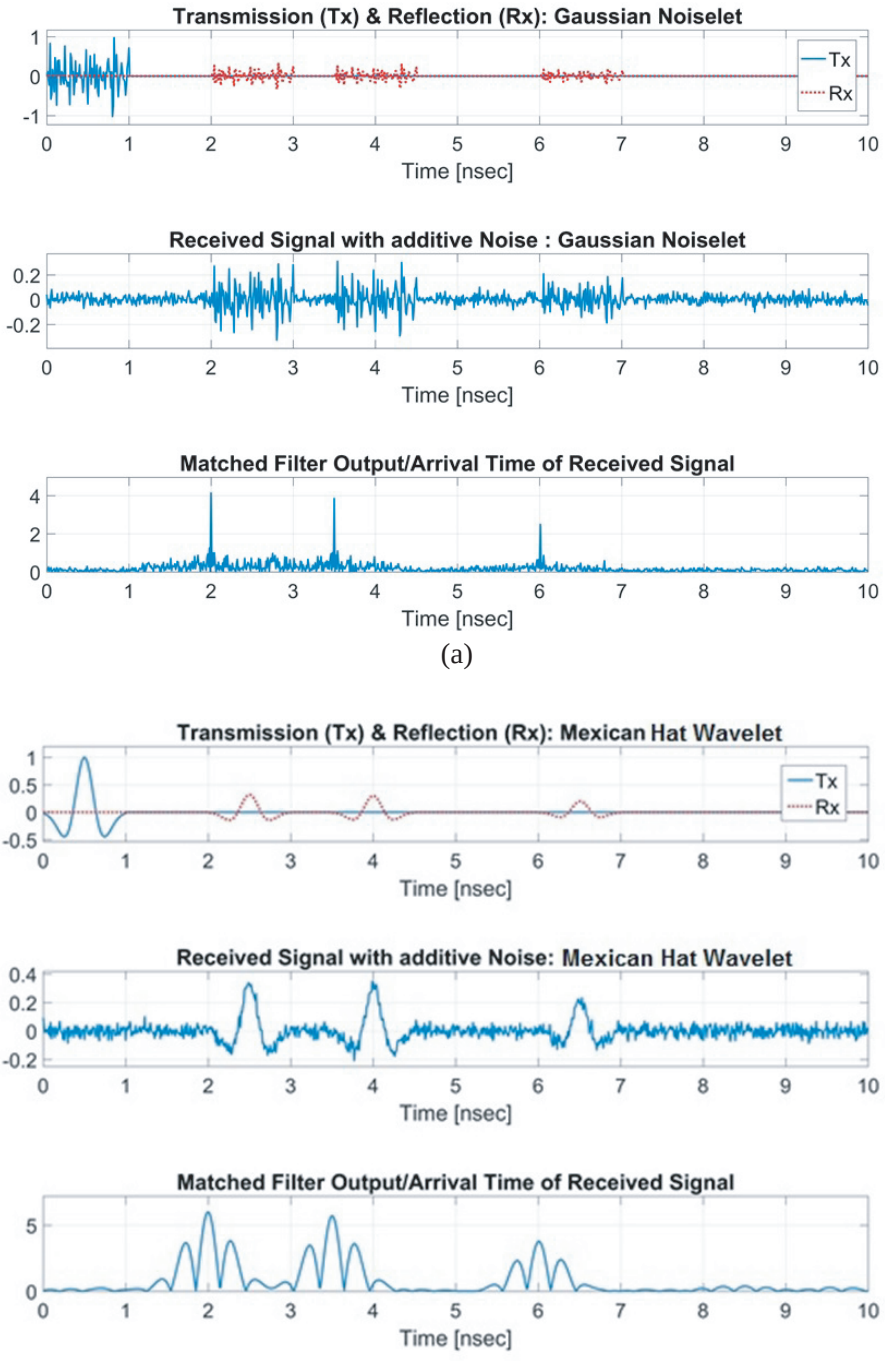

Figure 3. Arbitrary multiple target detection by using (a) random Gaussian noiselet, and (b) Mexican hat wavelet.

be noted that the sidelobes on the matched filter output for the Mexican hat wavelet may cause false detection or degradation of image resolution.

Figure 4 provides an enlarged view of first target over the 1–3 ns range for various values of SNR for both waveforms. The robustness of the Gaussian noiselet waveform over the traditional Mexican hat wavelet under added noise conditions is clearly noted since the peak correlation value is relatively unchanged for the former compared to the latter even at low SNRs.

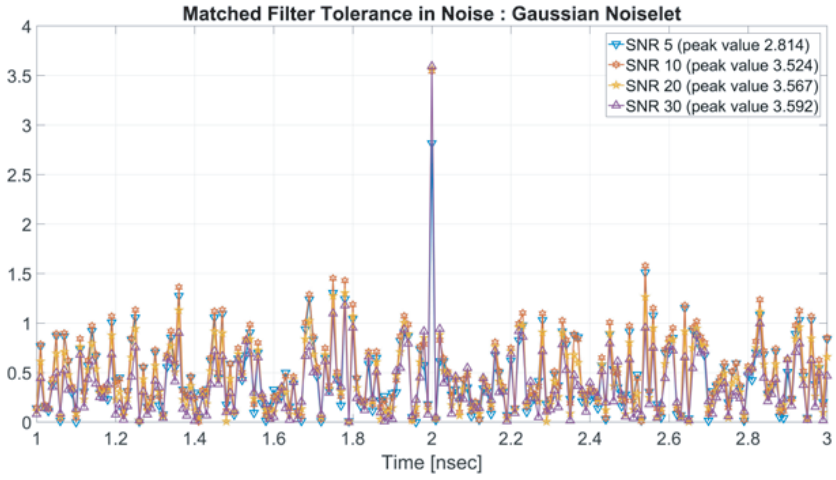

(a)

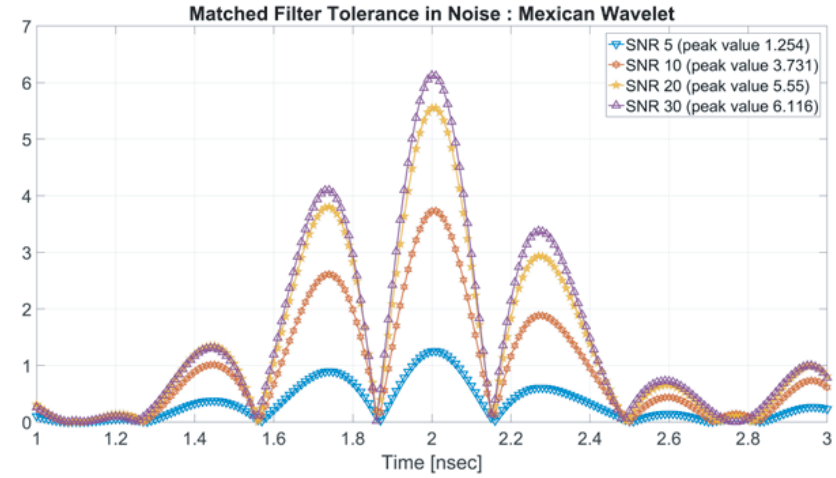

(b)

Figure 4. Performance under various SNR values for (a) random Gaussian noiselet, and (b) Mexican hat wavelet.

4. MULTILAYER SCATTERING

To understand the principal function of a microwave imaging system, it is important to briefly discuss how transmissions and reflections of traveling EM waves occur and propagate through various media interfaces. The thin layer shown in Fig. 5 is defined as the interface, or boundary, between medium 1 and 2. Assuming a uniform plane wave interacts with the boundary at normal incidence, it is seen that two phenomena occur — a portion of the EM wave is reflected back into medium 1, while another portion is transmitted into medium 2. Since every medium has unique material properties, transmission and reflection on each interface will provide information based on the boundary conditions.

The EM wave of Fig. 5 can be defined as a wave traveling in the z-direction. The coordinates of all figures and equations will be based on the same x-, y-, and z-direction coordinate system for consistency and simplicity of discussion. The electric fields in a transmission/reflection type EM model are given by the following expressions:

$$\vec{E}_i = \hat{y}E_0^i e^{-jk_1 z} \text{ (Incident wave)} \tag{5}$$

$$\vec{E}_t = \hat{y}E_0^t e^{-jk_2 z} \text{ (Transmitted wave)} \tag{6}$$

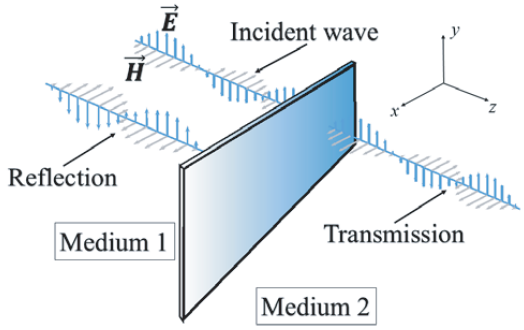

Figure 5. Uniform plane wave schematic at the interface between materials.

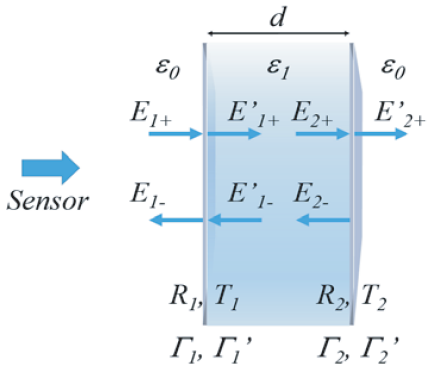

Figure 6. Wave propagation on interfaces for reflection data collection scheme.

$$\vec{E}_r = \hat{y}E_0^r e^{+jk_1 z} \text{ (Reflected wave)} \tag{7}$$

where $E_0^{i,t,r}$ is the corresponding amplitude of each wave, and $k_{1,2}$ is the corresponding wave number, which is based on the material properties of the media. The wave number is related to the angular frequency ω, permittivity ε, and permeability μ using [25]

$$k_i = \omega\sqrt{\varepsilon_i \mu_i} \tag{8}$$

Since the uniform plane waves travel between interfaces of each media, transmission and reflection should be expressed based on the location of observation. As can be seen in Fig. 6, the sensor is placed on the left side of the sample so that the system will collect the total reflected wave from the specimen. It is to be noted that there are two boundaries: 1) air to material, and 2) material to air, which will lead to the total reflection, Γ_{total}, which may be obtained from

$$\Gamma_{\text{total}} = \frac{E_{1-}}{E_{1+}} = \frac{R_1 + R_2 e^{-2jk_1 d}}{1 + R_1 R_2 e^{-2jk_1 d}} = \frac{R_1 + R_2 e^{-2j\theta_1}}{1 + R_1 R_2 e^{-2j\theta_1}} \tag{9}$$

where R_1 and R_2 are the reflection coefficients of each interface, which are based on the relationship of the intrinsic impedance of materials with respect to the material properties.

The electrical length θ_i is proportional to the product of wavenumber k_i and physical thickness d of the dielectric layer as can be seen from Eq. (10). In general, the reflection coefficient R_i and the intrinsic impedance Z_i at the interface of the i-th and the $(i+1)$-th layer can be described as

$$R_i = \frac{Z_{i+1} - Z_i}{Z_{i+1} + Z_i}, \quad Z_i = \sqrt{\frac{\mu_i}{\varepsilon_i}}, \quad \theta_i = k_i d \tag{10}$$

Expanding to the case of multilayered or multi-interface materials, it can be easily obtained using the generalized propagation matrix for the i-th layer and derived as

$$\begin{bmatrix} E_{i+} \\ E_{i-} \end{bmatrix} = \frac{1}{T_i} \begin{bmatrix} 1 & R_i \\ R_i & 1 \end{bmatrix} \begin{bmatrix} e^{j\theta_i} & 0 \\ 0 & e^{-j\theta_i} \end{bmatrix} \frac{1}{T_{i+1}} \begin{bmatrix} 1 & R_{i+1} \\ R_{i+1} & 1 \end{bmatrix} \begin{bmatrix} E'_{(i+1)+} \\ 0 \end{bmatrix} \tag{11}$$

which results in an expression similar to Eq. (9) as

$$\Gamma_i = \frac{E_{i-}}{E_{i+}} = \frac{R_i + R_{i+1} e^{-2j\theta_i}}{1 + R_i R_{i+1} e^{-2j\theta_i}} \tag{12}$$

5. SYNTHETIC APERTURE RADAR (SAR) SCANNING

SAR is a widely used radar technique in airborne radar systems for two-dimensional mapping. Since the resolution of a radar is based on the aperture size of the radar, it is preferred to have antenna with a larger aperture diameter. However, there are limits of increased antenna size, especially while mounted to an aircraft. The SAR technique overcomes the limit of real aperture radar (RAR) by synthesizing

data from a relatively small aperture to create that of a much larger aperture [26]. Although SAR was originally introduced for airborne radar, it can be applied to alternative applications based on its synthetization scheme [27, 28]. For example, scanning a target may be achieved using railed system with an antenna attached.

Figure 7 presents an NDT SAR imaging system for investigating multilayered FRP composites, where x, y and z denote the length, height and depth (or distance) of the testing specimen, respectively. As can be seen, an antenna scans over the xy-plane with a standoff distance D along the z-axis — the direction of the traveling wave. This SAR system requires a horn or lens antenna having a focused beam with a narrow beamwidth impinging on the sample at normal incidence, i.e., an incident angle of zero degrees. The antenna begins the sensing procedure at its designated point of origin and acquires data based on the sampling interval satisfying the Nyquist sampling rate to avoid aliasing effects.

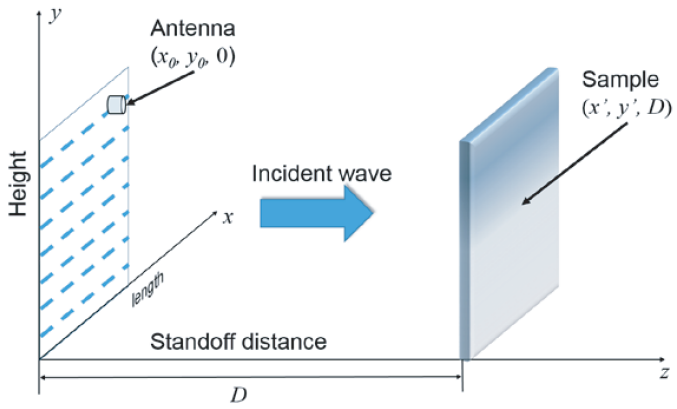

Figure 7. SAR NDT scanning geometry.

5.1. SAR Imaging Algorithm Using Range Migration Algorithm

In SAR processing, there are several techniques that may be applied to optimization and calibration of image processing, such as the range-Doppler algorithm (RDA), chirp scaling algorithm (CSA), range migration algorithm (RMA), just to name a few [26, 28]. Each algorithm has strengths and weaknesses based on the waveforms and testing conditions under which it is being conducted. Since our SAR NDT scanning is performed in the near-field range, and the specimens may be considered static targets, the range migration algorithm (RMA) provides the best choice to calibrate the received data. The near-field wavefront has a parabolic curvature by nature, hence, the received raw data will reflect with the opposite curvature compared to the original wavefront, as shown in Fig. 8.

The main feature of RMA is the exploitation of the Stolt interpolation technique [29, 30] which is the calibration process used to convert the received data into a plane wave. Stolt interpolation

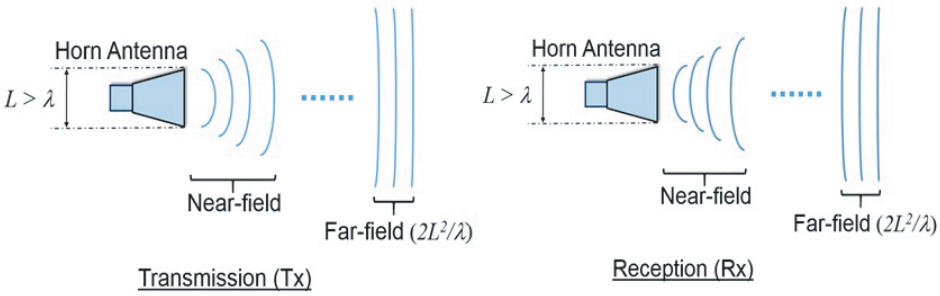

Figure 8. Transmitted and received signal in near-field and far-field ranges.

was originally introduced in geology for processing seismic data. Since the wavefront for seismic data collection is similar to near-field SAR techniques, Stolt interpolation is applicable for optimization and calibration of received raw data.

Since the Stolt interpolation is executed on the frequency domain data, a Fourier transform of received time domain data should be performed before applying this calibration process. Back to RMA — the coordinate references from Fig. 7 will be used for theoretical expansion. This expansion will be based on a single point of specimen, which will form an image data matrix once the data has been gathered at each sample point. Here, the reflection coefficient can be written as $R(x, y, z)$ and the reflected raw data will be $s_r(x_0, y_0, k_r)$, where k_r is the wavenumber based on the operating frequency. The reflected raw signal can be represented as

$$s_r(x_0, y_0, k_r) \approx R(x, y, z) \cdot e^{jk_r D} \cdot e^{-jk_r D_t} \tag{13}$$

where D is the standoff distance between antenna and specimen, and D_t is the distance from antenna to arbitrary target point. D_t can be expressed as

$$D_t = \sqrt{(x_0 - x)^2 + (y_0 - y)^2 + (-D - z)^2} \tag{14}$$

In Eq. (13), there are two exponential terms: the first term is the reference phase between the antenna and normal incident interface of specimen, while the second term represents the phase information from the arbitrary point of specimen.

Since it is already mentioned that domain transformation is necessary, the reflected raw signal s_r can be transferred from time- to wavenumber-domain using the Fourier transform so that S_r can be derived as

$$S_r(k_x, k_y, k_r) = R(x, y, z) \iint e^{jk_r D} \cdot e^{-jk_r D_{\text{target}}} \cdot e^{-jk_x x_0} \cdot e^{-jk_y y_0} dx_0 dy_0 \tag{15}$$

Using the stationary phase approximation, the result is

$$S_r(k_x, k_y, k_r) = R(x, y, z) \cdot e^{jk_r D} \cdot e^{-j\sqrt{k_r^2 - k_x^2 - k_y^2} \cdot (z+D)} \cdot e^{-jk_x x} \cdot e^{-jk_y y} \tag{16}$$

Eq. (16) can be rearranged for matched filtering to yield

$$S_r(k_x, k_y, k_r) = R(x, y, z) \cdot e^{j\left(k_r - \sqrt{k_r^2 - k_x^2 - k_y^2}\right)D} \cdot e^{-j\left(k_x x + k_y y + \sqrt{k_r^2 - k_x^2 - k_y^2} \cdot z\right)} \tag{17}$$

Similarly, the transmitted signal after Fourier transformation and matched filtering can be expressed as

$$S_{mf}(k_x, k_y, k_r) = S_t \cdot S_r \approx \left(k_r - \sqrt{k_r^2 - k_x^2 - k_y^2}\right) \cdot D \tag{18}$$

following which Stolt interpolation can be applied to optimization and calibration to correct for the wavefront curvature, resulting in $S_{st}(k_x, k_y, k_z)$. After Stolt interpolation, the relationship between time-domain coordinates (x, y, z) and wavenumbers (k_x, k_y, k_z) is linearized so that it can be applied to image reconstruction, which is the final goal of our SAR NDT imaging system.

6. APPLICATION OF MULTIRESOLUTION RF NOISELETS

6.1. Analytical Considerations in Multiresolution Imaging

RF noiselets have several advantages in multiresolution radar detection and imaging applications. An application being considered here is nondestructive testing (NDT) of multilayered structures. Since the range resolution is inversely proportional to the bandwidth, images at different resolutions can be obtained by processing the return at different bandwidth values. This can be accomplished by transmitting an RF noiselet with the maximum bandwidth for the highest resolution, and then degrading the bandwidth progressively to obtain coarser resolutions. While achieving the best resolution enables the detection of small and thin defects in multilayered structures, it is also important to characterize the structure in the vicinity of the detected defect. This is important as more information on the defect, such as its full extent and possible growth, can be gleaned by examining not only the defect image at the highest resolution but also by simultaneously examining images at coarser resolution in its proximity.

Consider two multilayered structures A and B each having an identical linear defect, such as a disbond or a delamination, perpendicular to the direction of wave propagation. Let the dielectric constant of the defect be denoted as ε_{rd} and its thickness d be exactly equal to the resolution obtained from the maximum bandwidth B, i.e., assume $d = \Delta R = c/2B\sqrt{\varepsilon}_r$, in both cases. Further, we assume that the range bin is placed at the center of the defect at depth coordinate $z = z_0$. Thus, for the highest resolution case, the average dielectric constant around $z = z_0$ that determines the scattering from the defect layer is easily deduced as $\overline{\varepsilon_{rA}(z_0, B)} = \overline{\varepsilon_{rB}(z_0, B)} = \varepsilon_{rd}$ for both structures.

Now, we make a distinction between the two multilayered structures A and B for the dielectric constant profiles as a function of depth z above and below the defect layer. Let the dielectric constant profile for structure A be given by

$$\varepsilon_{rA}(z) = \begin{cases} \varepsilon_{rAl}(z), & z < z_0 - \dfrac{d}{2} \\ \varepsilon_{rd}, & z_0 - \dfrac{d}{2} \le z \le z_0 + \dfrac{d}{2} \\ \varepsilon_{rAu}(z), & z > z_0 + \dfrac{d}{2} \end{cases} \tag{19}$$

where the subscripts l and u denote lower and upper layers with respect to the position of the defect.

Similarly, let the dielectric constant profile of structure B be given by

$$\varepsilon_{rB}(z) = \begin{cases} \varepsilon_{rBl}(z), & z < z_0 - \dfrac{d}{2} \\ \varepsilon_{rd}, & z_0 - \dfrac{d}{2} \le z \le z_0 + \dfrac{d}{2} \\ \varepsilon_{rBu}(z), & z > z_0 + \dfrac{d}{2} \end{cases} \tag{20}$$

It is important to note that, in general, $\varepsilon_{rAl}(z) \neq \varepsilon_{rBl}(z)$ and $\varepsilon_{rAu}(z) \neq \varepsilon_{rBu}(z)$.

If the resolution is degraded by a factor of 2 using a bandwidth of $B/2$ resulting in a depth resolution of $2d$, then the average dielectric constants of structures A and B around $z = z_0$ are given by, respectively,

$$\overline{\varepsilon_{rA}\left(z_0, \frac{B}{2}\right)} = \frac{1}{2d}\int_{z_0-d}^{z_0+d} \varepsilon_{rA}(z)dz = \frac{1}{2d}\int_{z_0-d}^{z_0-d/2} \varepsilon_{rAl}(z)dz + \frac{\varepsilon_{rd}}{2} + \frac{1}{2d}\int_{z_0+d/2}^{z_0+d} \varepsilon_{rAu}(z)dz \tag{21}$$

and

$$\overline{\varepsilon_{rB}(z_0, \frac{B}{2})} = \frac{1}{2d}\int_{z_0-d}^{z_0+d} \varepsilon_{rB}(z)dz = \frac{1}{2d}\int_{z_0-d}^{z_0-d/2} \varepsilon_{rBl}(z)dz + \frac{\varepsilon_{rd}}{2} + \frac{1}{2d}\int_{z_0+d/2}^{z_0+d} \varepsilon_{rBu}(z)dz \tag{22}$$

Since the average dielectric constants given by Eqs. (21) and (22) will in general be unequal owing to the fact that $\varepsilon_{rAl}(z) \neq \varepsilon_{rBl}(z)$ and $\varepsilon_{rAu}(z) \neq \varepsilon_{rBu}(z)$, the images at a bandwidth of $B/2$ will be different for each structure.

Similarly, if the resolution is degraded by a factor of $N \geq 1$ using a bandwidth of B/N resulting in a depth resolution of Nd, then the average dielectric constants of structures A and B around $z = z_0$ are given by, respectively,

$$\overline{\varepsilon_{rA}\left(z_0, \frac{B}{N}\right)} = \frac{1}{Nd}\int_{z_0-Nd/2}^{z_0+Nd/2} \varepsilon_{rA}(z)dz = \frac{1}{Nd}\int_{z_0-Nd/2}^{z_0-d/2} \varepsilon_{rAl}(z)dz + \frac{\varepsilon_{rd}}{N} + \frac{1}{Nd}\int_{z_0+d/2}^{z_0+Nd/2} \varepsilon_{rAu}(z)dz \tag{23}$$

and

$$\overline{\varepsilon_{rB}(z_0, \frac{B}{N})} = \frac{1}{Nd}\int_{z_0-Nd/2}^{z_0+Nd/2} \varepsilon_{rB}(z)dz = \frac{1}{Nd}\int_{z_0-Nd/2}^{z_0-d/2} \varepsilon_{rBl}(z)dz + \frac{\varepsilon_{rd}}{N} + \frac{1}{Nd}\int_{z_0+d/2}^{z_0+Nd/2} \varepsilon_{rBu}(z)dz \tag{24}$$

We note again that the average dielectric constants given by Eqs. (23) and (24), and the corresponding images at a bandwidth of B/N will be different for each structure.

By exploring the images at various resolutions, fine to coarse, the complete information on the defect and its vicinity can be obtained for a better characterization of the defect region and its surrounding regions.

6.2. Multiresolution Image Formation

Four different structures (ST1–ST4) were investigated for multiresolution analysis, as shown in Fig. 9. Each structure contains two airgaps surrounding the central dielectric region. The shaded regions in Fig. 9 are assumed to be a lossless dielectric of dielectric constant $\varepsilon_r = 4$. The thicknesses of the airgaps and the central dielectric region are different in each structure. Table 1 lists the bandwidths used for image generation and the corresponding resolutions obtained. Waveforms used for comparison were the Gaussian noiselet and the Mexican Hat wavelet.

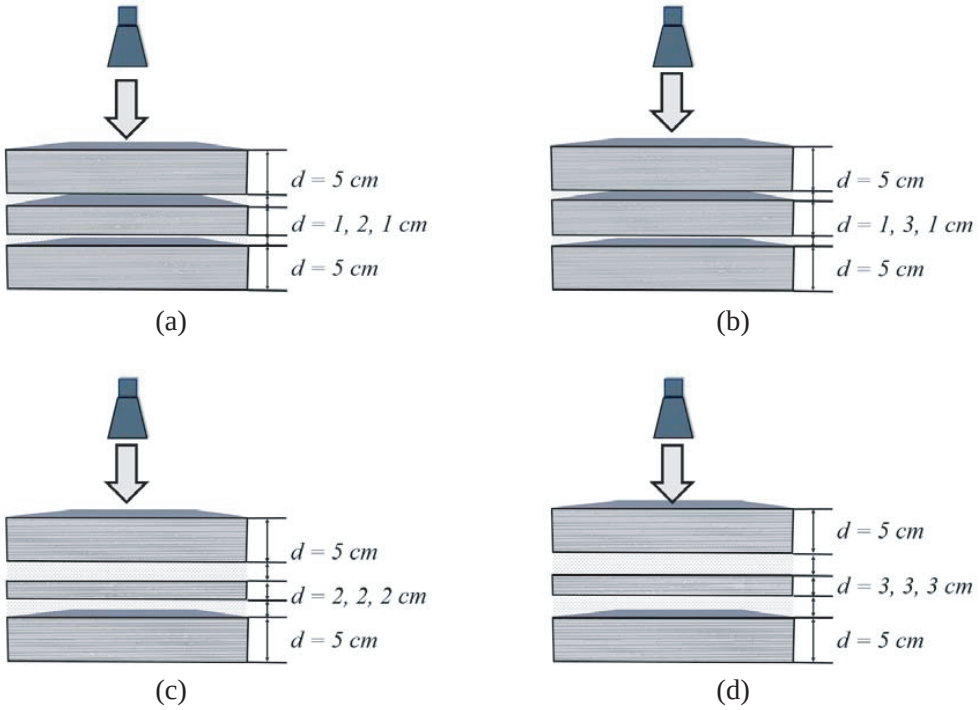

Figure 9. Defect structures investigated for multiresolution analysis. (a) ST1, (b) ST2, (c) ST3, and (d) ST4.

Table 1. Bandwidths and resolutions investigated.

Frequency range (GHz)	Bandwidth (GHz)	Depth resolution for $\varepsilon_r = 4$ (cm)
8–12	4	1.875
8.5–11.5	3	2.5
9–11	2	3.75
9.5–10.5	1	7.5

Figures 10–13 show the images obtained for all four structures using both waveforms at different resolutions for structures ST1–ST4, respectively.

From Figs. 10–13, we note that the image resolutions depends on the signal bandwidth for both waveforms. Furthermore, the images get blurred as the resolution degrades by decreasing the bandwidth, as expected [31]. We also note that the images corresponding to each waveform are similar for the same structure at the same resolution.

Several images, however, show noticeable differences between both waveforms, especially for the 2-GHz bandwidth results, as observed in Figs. 10(c)–13(c). Furthermore, the reconstructed images with the Gaussian noiselet appears to be providing relatively finer and more accurate results compared to the images using the wavelet waveform. Note from Fig. 11 images of structure ST2, both waveforms

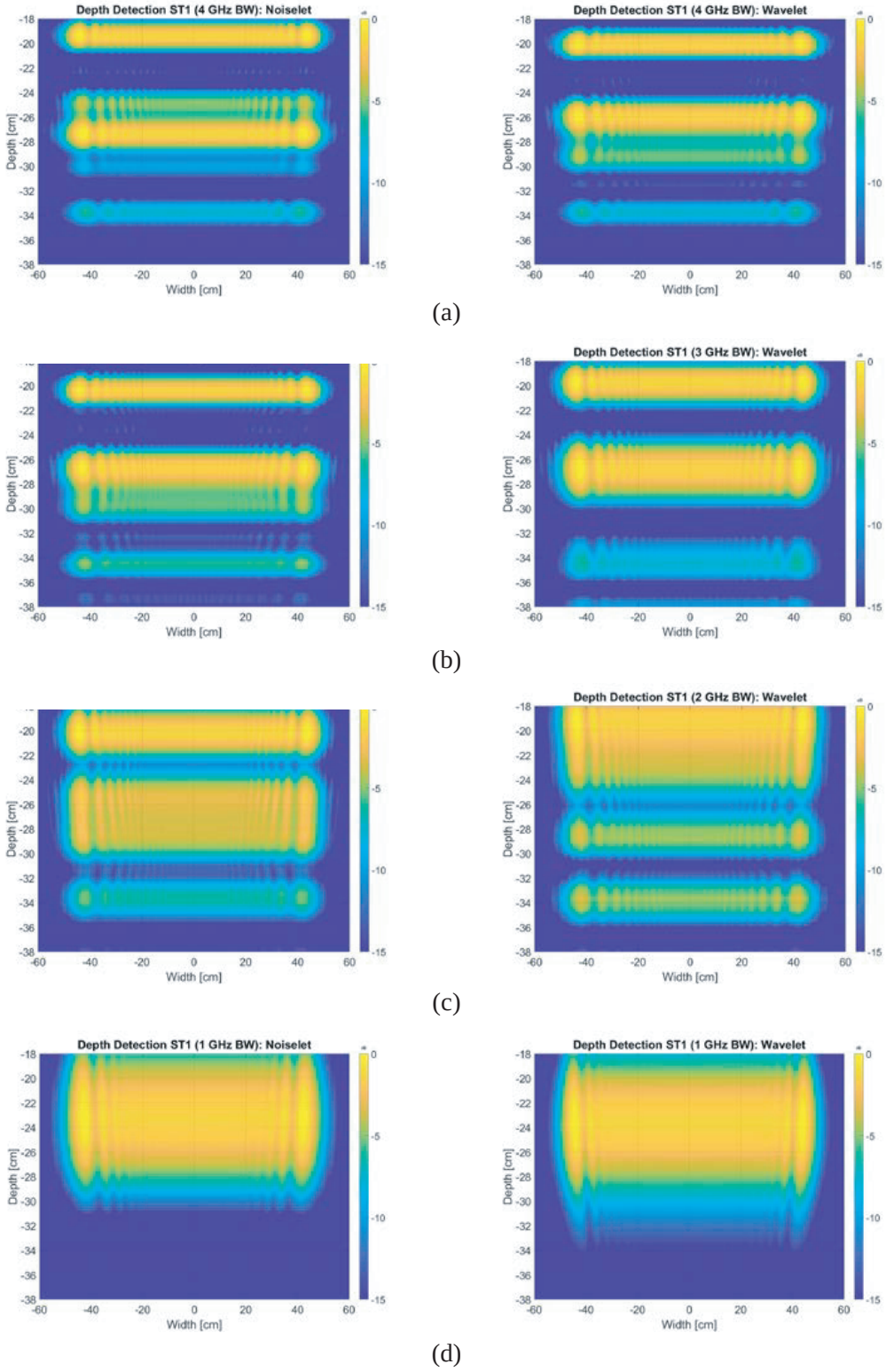

Figure 10. Reconstructed image for ST1 for Gaussian noiselet (left) and Mexican Hat wavelet using bandwidth of (a) 4 GHz, (b) 3 GHz, (c) 2 GHz, and (d) 1 GHz.

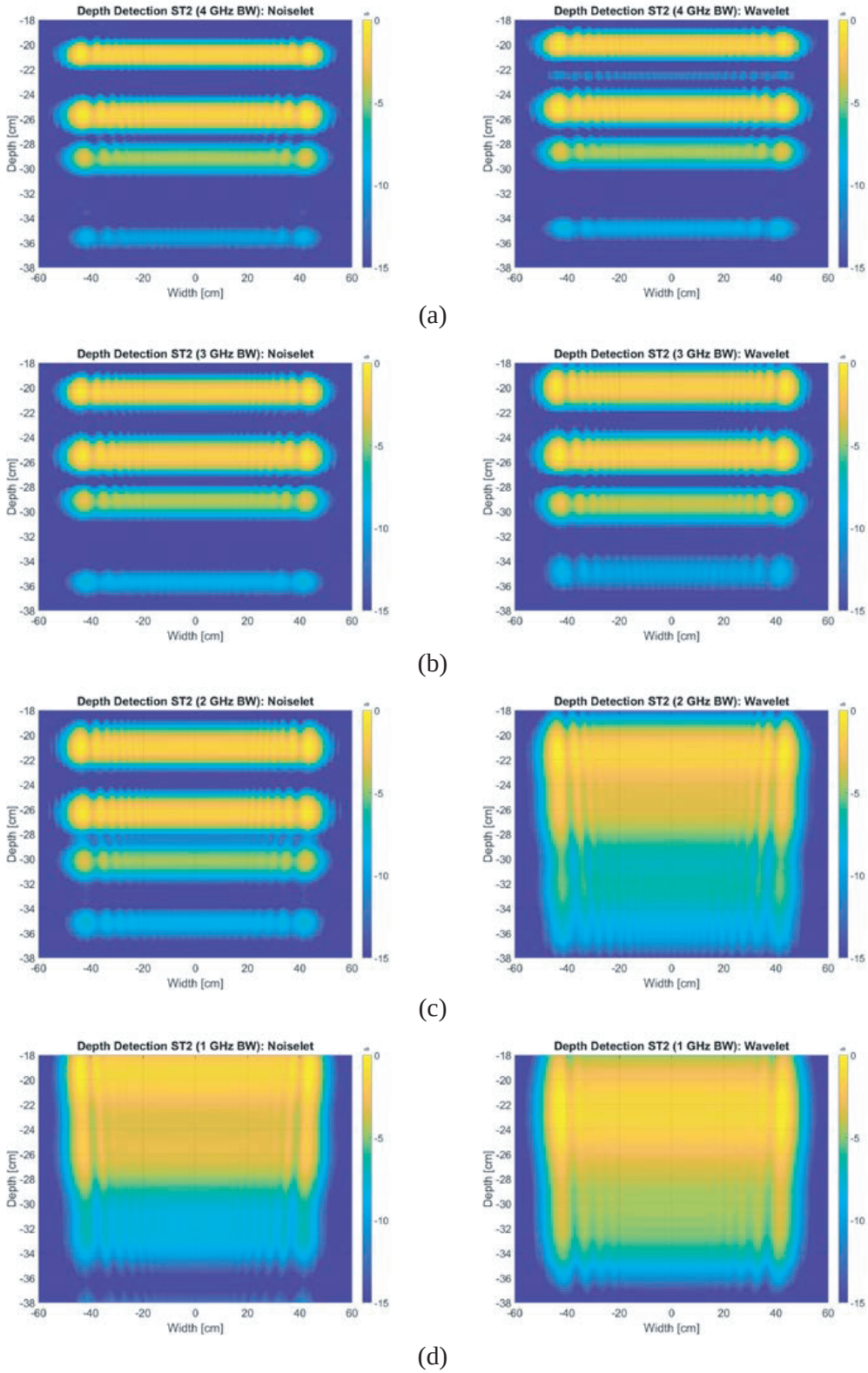

Figure 11. Reconstructed image for ST2 for Gaussian noiselet (left) and Mexican Hat wavelet using bandwidth of (a) 4 GHz, (b) 3 GHz, (c) 2 GHz, and (d) 1 GHz.

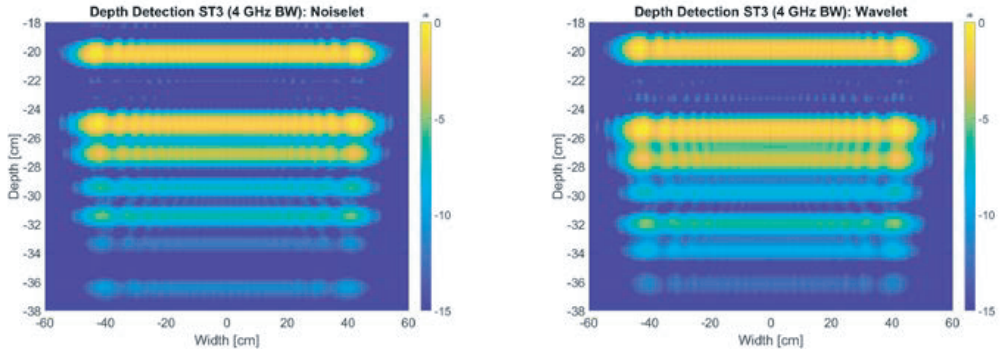

(a)

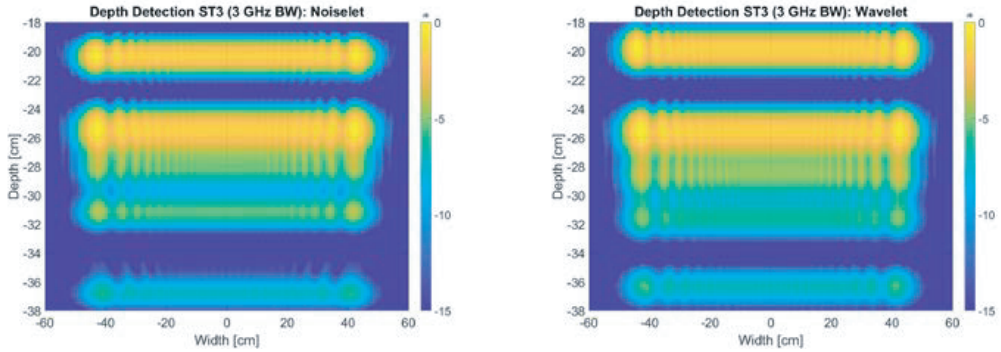

(b)

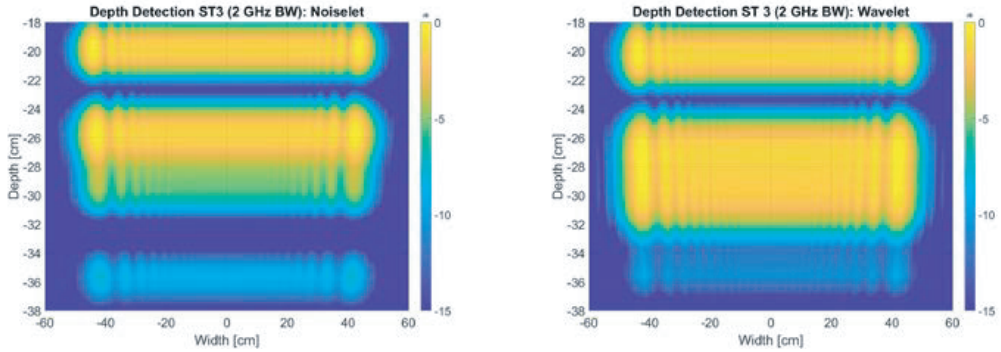

(c)

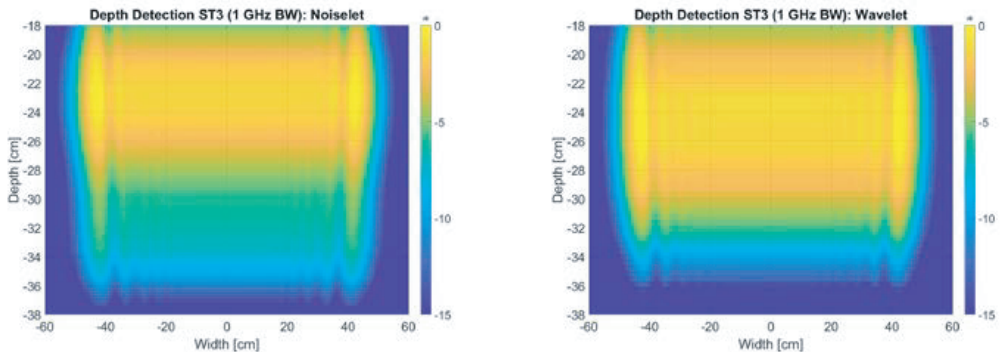

(d)

Figure 12. Reconstructed image for ST3 for Gaussian noiselet (left) and Mexican Hat wavelet using bandwidth of (a) 4 GHz, (b) 3 GHz, (c) 2 GHz, and (d) 1 GHz.

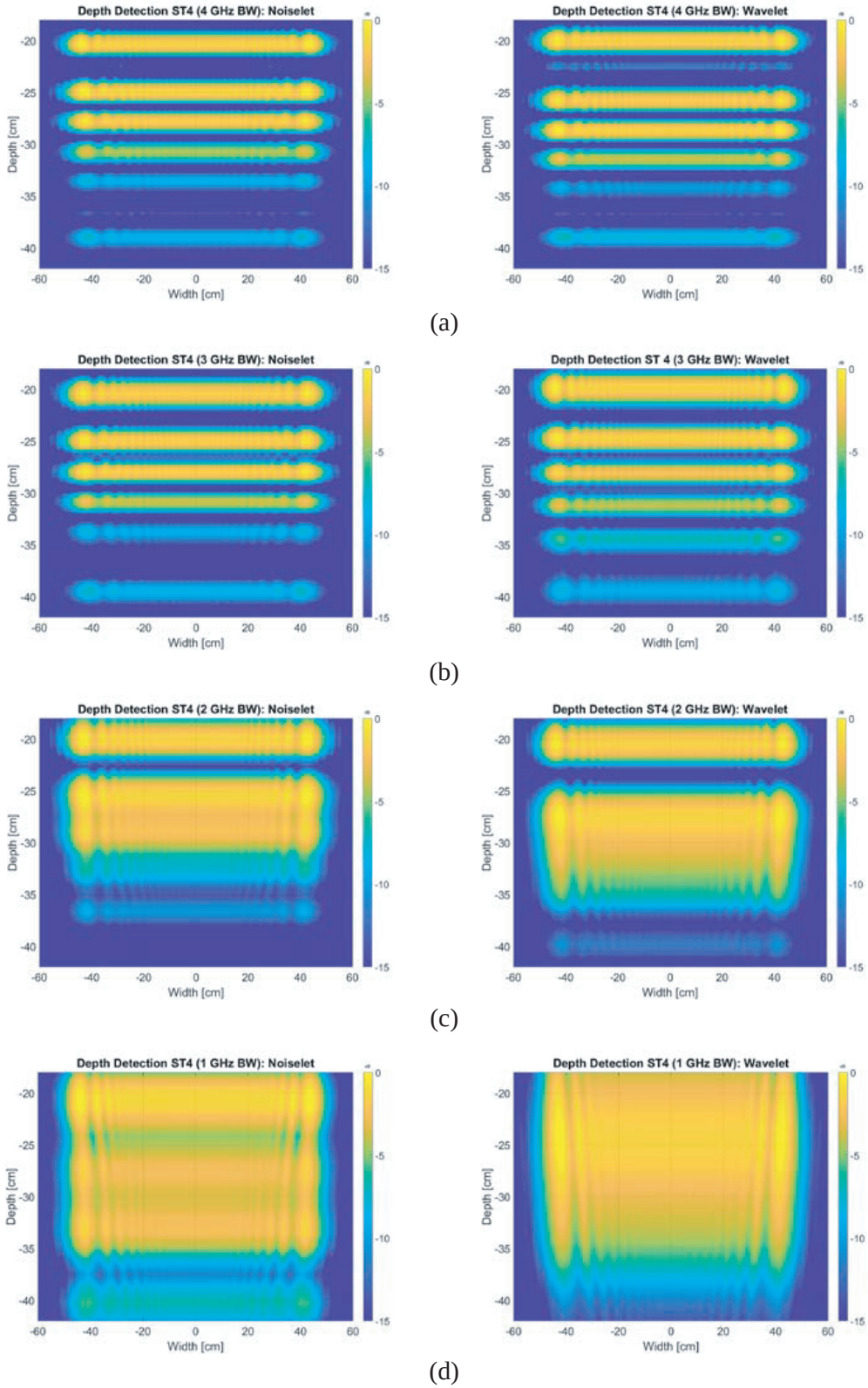

Figure 13. Reconstructed image for ST4 for Gaussian noiselet (left) and Mexican Hat wavelet using bandwidth of (a) 4 GHz, (b) 3 GHz, (c) 2 GHz, and (d) 1 GHz.

show relatively poor results which might be a critical structure for both noiselet and wavelet waveforms to resolve or indicate the structure condition precisely.

Although differences in reconstructed images denote that the noiselet waveform could provide better resolutions or results, we need to quantitatively verify that the noiselet waveform is more advantageous. Moreover, we also need to conform that the frequency bandwidth variation would serve as a powerful potential tool using noiselet waveforms for multiresolution analysis.

6.3. Image Similarity Analysis

To perform multiresolution analysis, we propose an image comparison algorithm to measure the similarity between images at various resolutions. By comparing the correlations between images at different resolutions, it can be assessed whether the degraded image retains or suppresses information relative to the target structure. For this analysis, the raw pixel values were used, not the dB values shown in Figs. 10–13. The notation $x(i,j)$ is used for the reference image and $y(i,j)$ for the image to be compared, where i and j are the location of each measurement point or pixel, and x and y denote the bandwidth in GHz (1–4). Normalization is performed based on following relation to obtain the correlation coefficients $C_{xy}(i,j)$, given by

$$C_{xy}(i,j) = \begin{cases} \dfrac{x(i,j)}{y(i,j)} \forall\, x(i,j) < y(i,j) \\ \dfrac{y(i.j)}{x(i,j)} \forall\, y(i,j) < x(i,j) \\ 1 \forall\, x(i,j) = y(i,j) \end{cases} \tag{25}$$

This ensures that the pixel-to-pixel correlation coefficients vary between 0 and 1. The total normalized similarity index between the images, S_{xy}, is obtained by averaging the pixel-to-pixel correlation

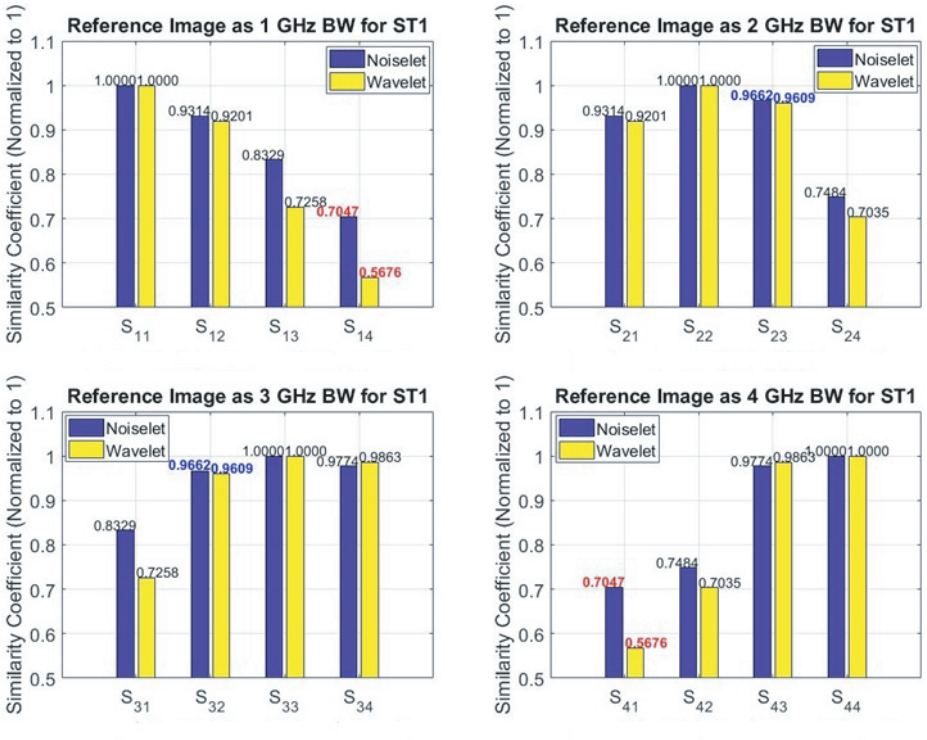

Figure 14. Similarity indices for structure ST1 for different reference images.

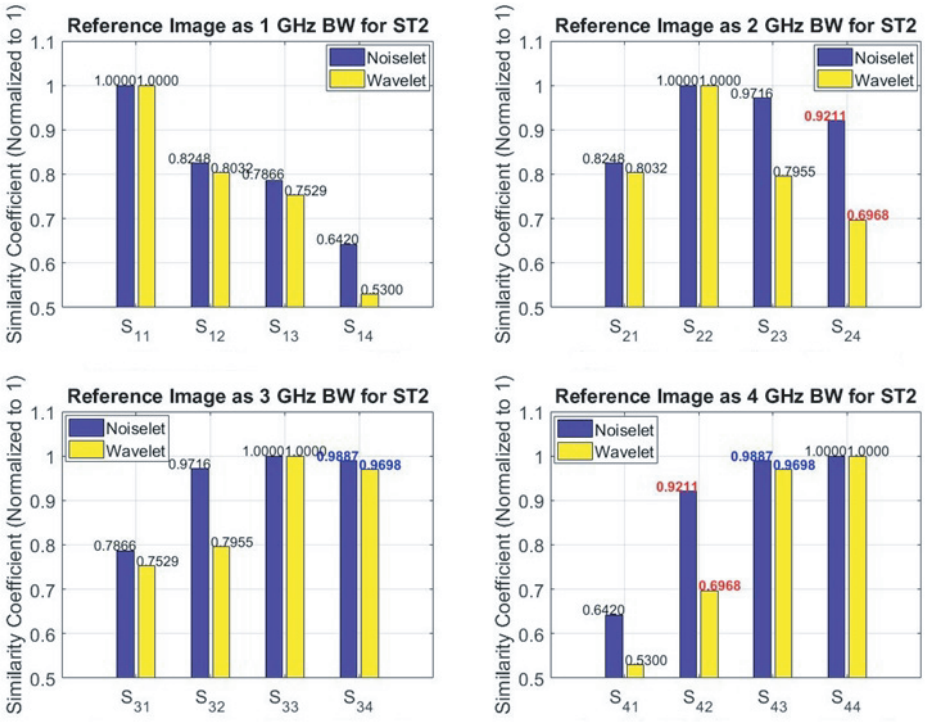

Figure 15. Similarity indices for structure ST2 for different reference images.

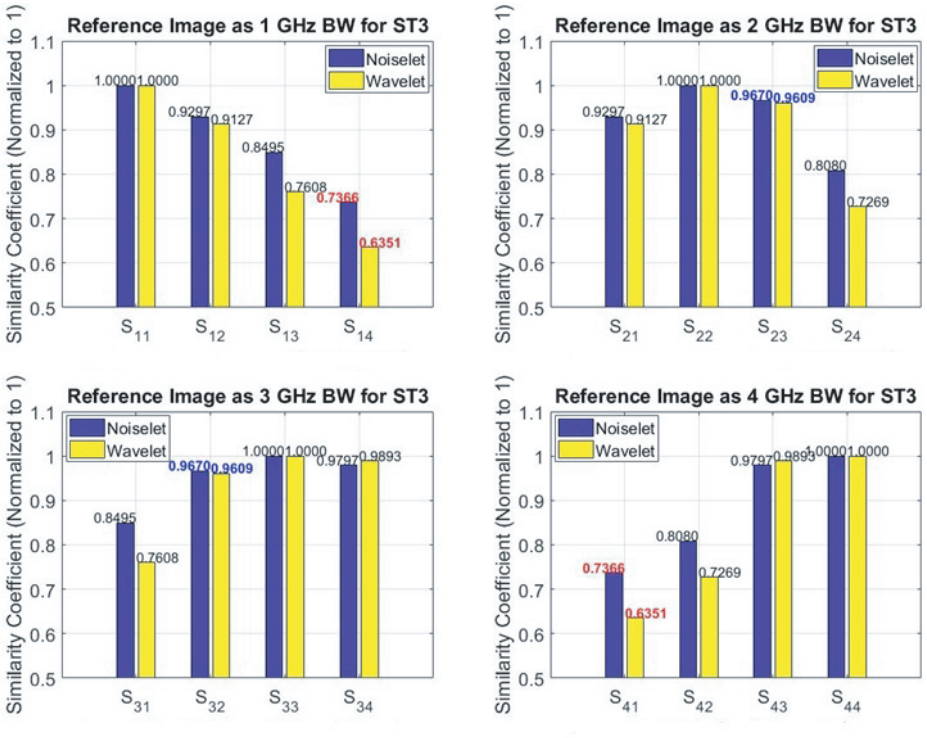

Figure 16. Similarity indices for structure ST3 for different reference images.

coefficients over the entire image, using

$$S_{xy} = \frac{\sum_{j=1}^{m} \sum_{i=1}^{n} C_{xy}(i,j)}{m \times n} \tag{26}$$

where m and n are the total numbers of pixels in the two directions of the 2-dimensional image. In our case, $m = n = 1024$. The similarity factors were obtained by comparing the image data pertaining to 1, 2, 3, and 4 GHz bandwidth signals. Obviously, $S_{11} = S_{22} = S_{33} = S_{44} = 1$, and $S_{xy} = S_{yx}$. Also, there are a total of six (6) similarity indices with values less than unity.

Figures 14–17 show the similarity indices for structures ST1–ST4, respectively. In these figures, values shown in color depict the largest (red) and the lowest (blue) difference in similarity indices between the values using the noiselet and the wavelet waveforms. We also note that as the bandwidth difference increases, the corresponding similarity index decreases. In general, the similarity indices for the noiselet waveform are higher than that of the wavelet waveform, indicating that the noiselet waveform is better able to associate or relate images at varying resolutions for the same structure.

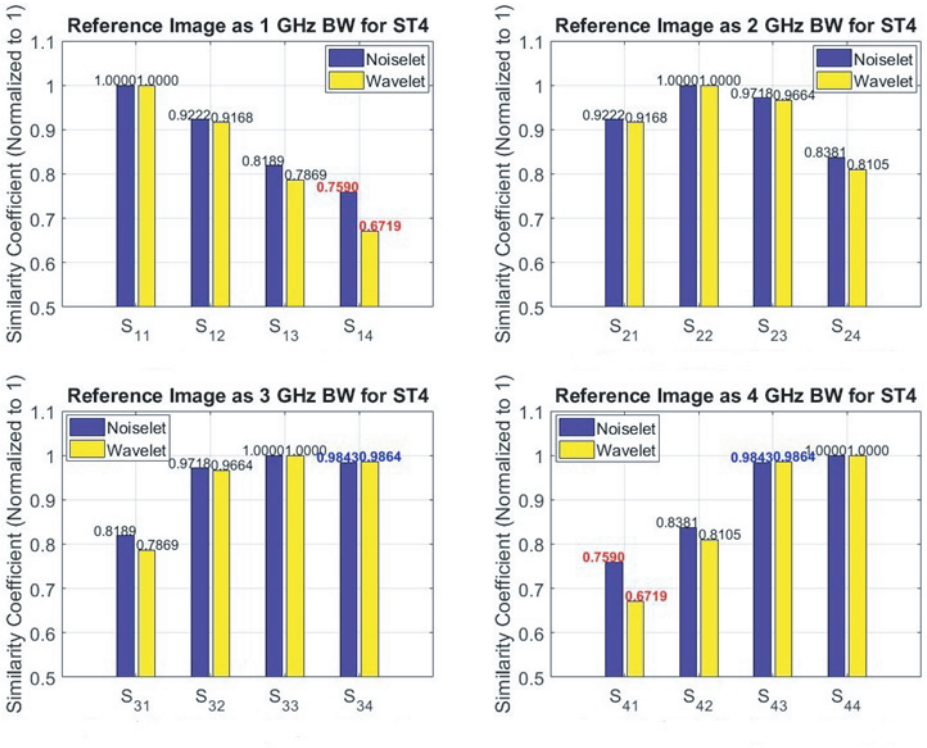

Figure 17. Similarity indices for structure ST4 for different reference images.

Figures 18 and 19 show the similarity coefficients for the nearest neighbors and the farthest neighbors, respectively. Similarity coefficients for nearest neighbors are S_{12}, S_{23}, and S_{34}, while those for farthest neighbors are S_{14} (for the 1 and 4 GHz images), S_{13} (for the 3 GHz image), and S_{24} (for the 2 GHz image). As can be seen, the nearest neighbor trends show that not much of information is lost when comparing the images of nearest bandwidth pairs. However, the far neighbor trends indicate that the noiselet waveform associates more information between images of differing resolutions when compared to the wavelet waveform.

Note from Figs. 15, 18 and 19 that the results on ST2 provide slightly different trends from other structures, as stated earlier. This is also suggested from the fact that the largest differences are observed for S_{24} while others show the largest difference for S_{14}, as expected.

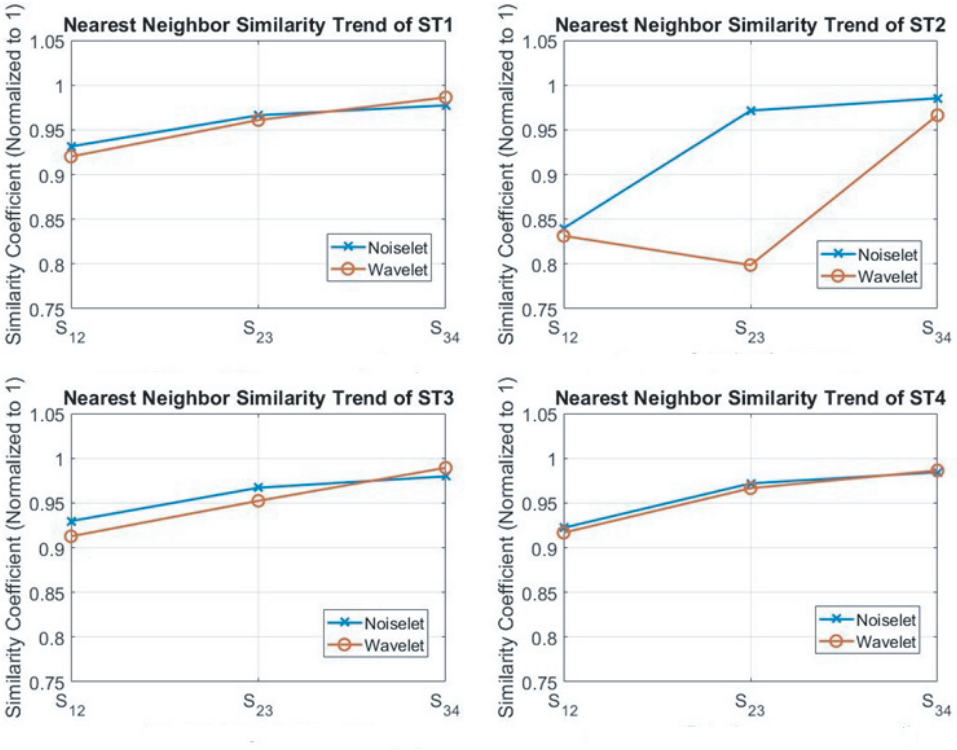

Figure 18. Similarity coefficient trends for nearest neighbors for various structures.

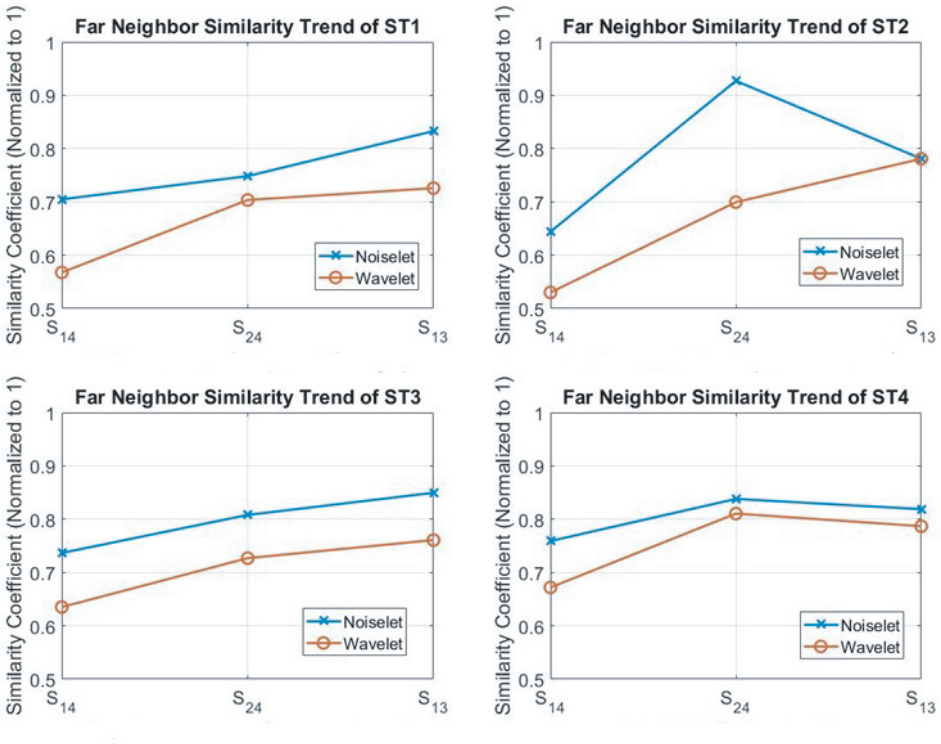

Figure 19. Similarity coefficient trends for farthest neighbors for various structures.

6.4. Difference Image Analysis

Having established above that the noiselet waveform better preserves structural information across images of varying resolutions, it would be worthwhile to visualize the correlation data to emphasize the area which has more similarity.

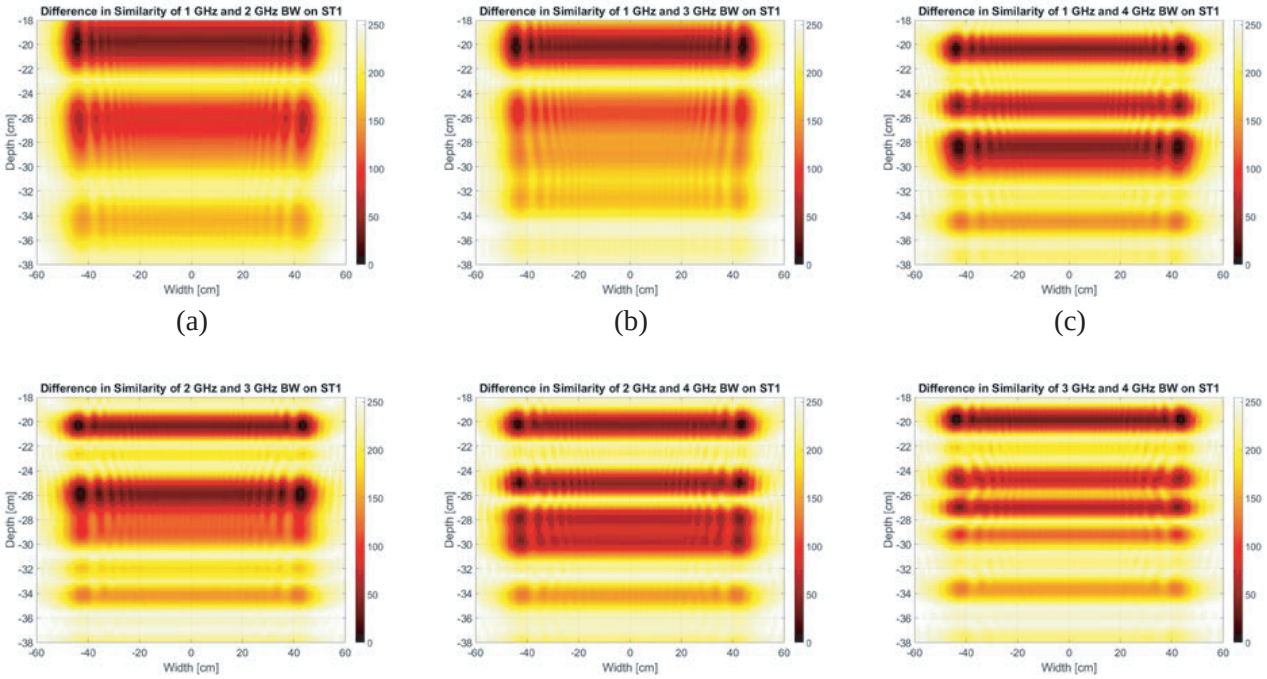

Figure 20. Difference images for ST1. (a) Δ_{12}, (b) Δ_{13}, (c) Δ_{14}, (d) Δ_{23}, (e) Δ_{24}, and (f) Δ_{34}.

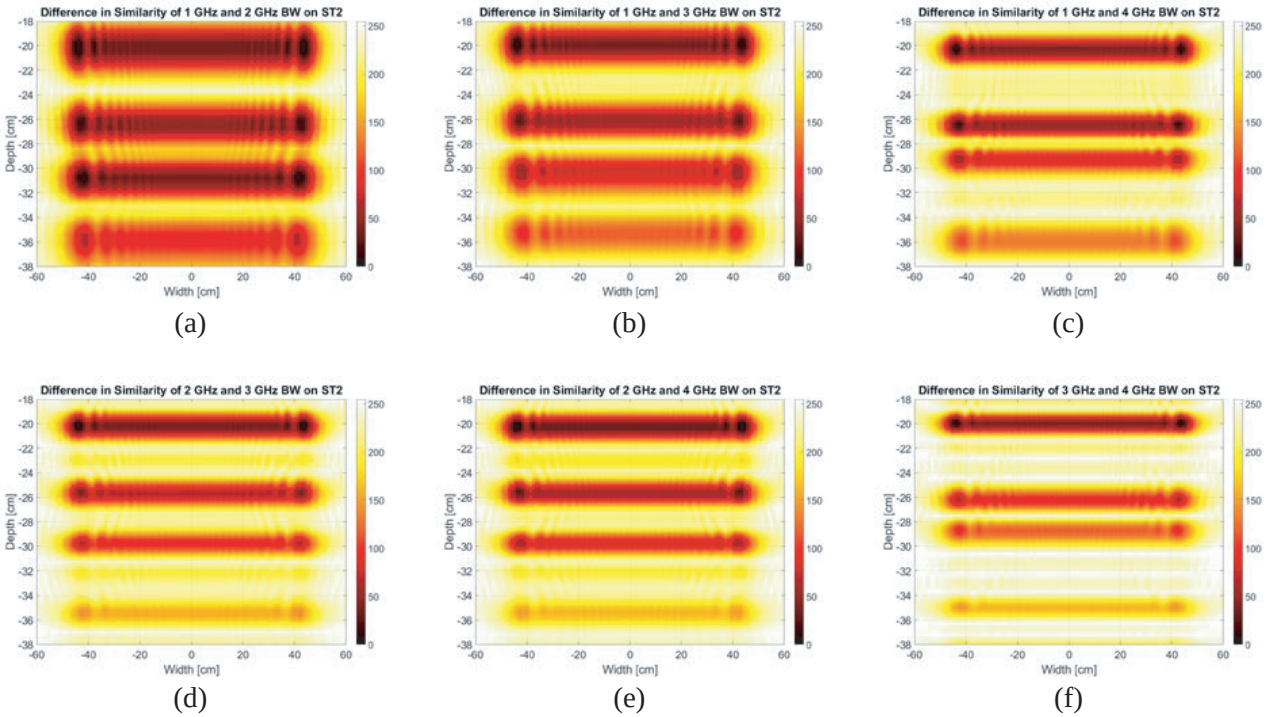

Figure 21. Difference images for ST2. (a) Δ_{12}, (b) Δ_{13}, (c) Δ_{14}, (d) Δ_{23}, (e) Δ_{24}, and (f) Δ_{34}.

A simple technique, which we call the modified difference mapping of reflection data, is performed to identify the higher-valued correlated areas for image comparison for several bandwidth combinations. In the modified difference image, each pixel value is based on following relation

$$\Delta_{xy}(i,j) = |\log x(i,j) - \log y(i,j)| \; \forall \, i, \; j \tag{27}$$

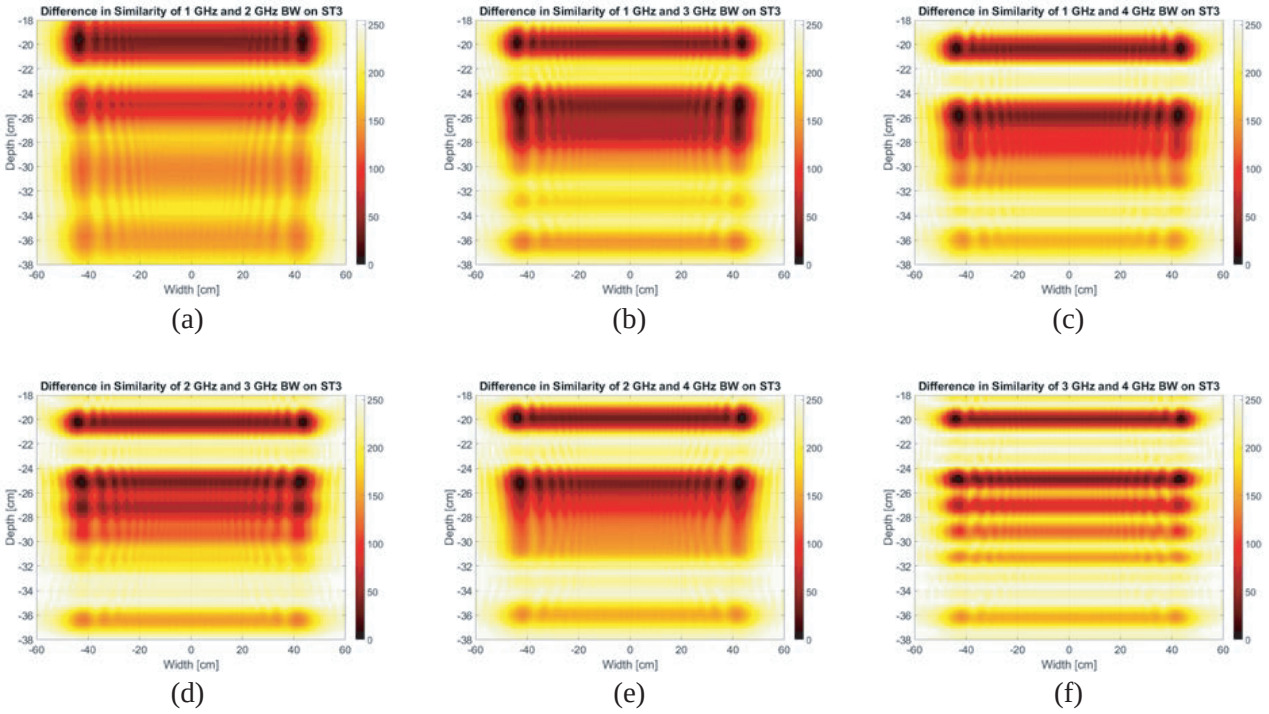

Figure 22. Difference images for ST3. (a) Δ_{12}, (b) Δ_{13}, (c) Δ_{14}, (d) Δ_{23}, (e) Δ_{24}, and (f) Δ_{34}.

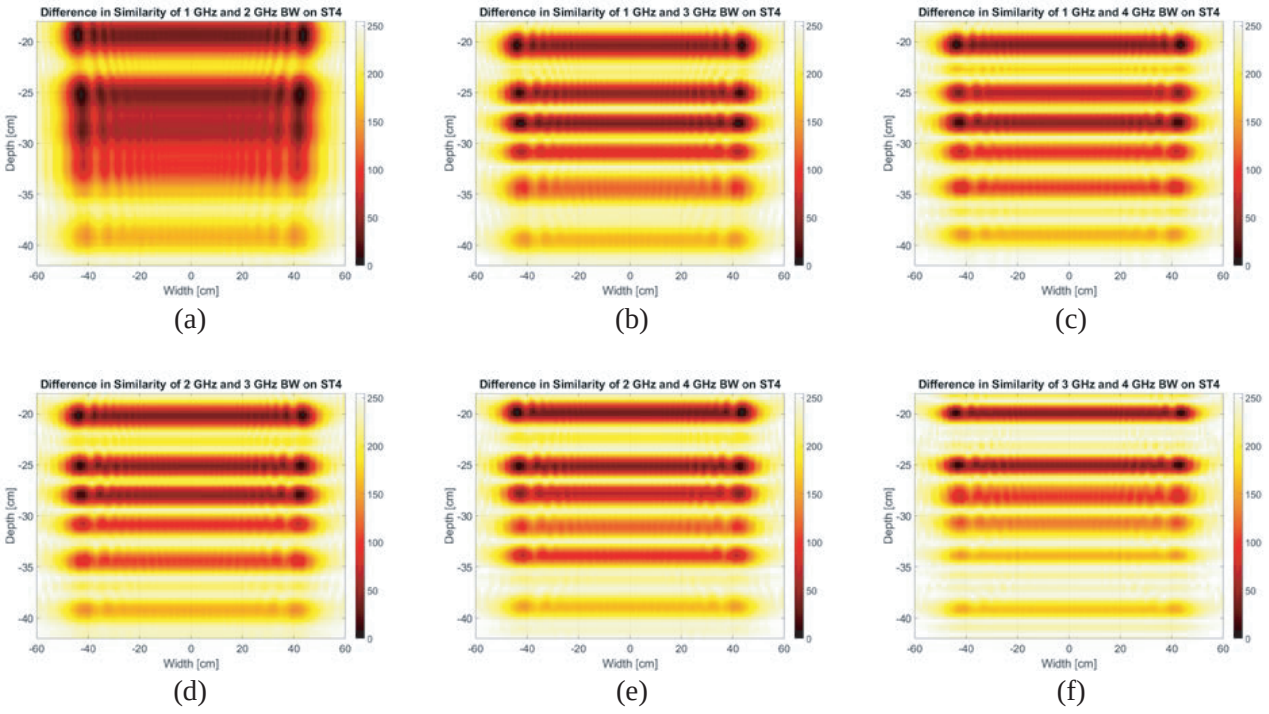

Figure 23. Difference images for ST4. (a) Δ_{12}, (b) Δ_{13}, (c) Δ_{14}, (d) Δ_{23}, (e) Δ_{24}, and (f) Δ_{34}.

Next, the gray scale is applied after normalizing to a 0–255 scale, as follows

$$\Delta_{xy,\,\text{grayscale}} = \frac{|\Delta_{xy}(i,j)|}{\max|\Delta_{xy}(i,j)|} \times 255 \tag{28}$$

Thus, a value of 0 indicates the lowest difference (highest similarity) while a value of 255 indicates highest difference (lowest similarity).

A total of six (6) images are possible for each structure using the four (4) bandwidths, namely, Δ_{12}, Δ_{13}, Δ_{14}, Δ_{23}, Δ_{24}, and Δ_{34}. These six images, converted to grayscale and rendered in color for clarity, were generated for all four structures ST1–ST4. Figs. 20–23 show these images for ST1–ST4, respectively.

The difference mapping of Δ_{34} provides the best resolution, as expected, due to the combination of larger bandwidths. Interestingly, Δ_{14} (or even Δ_{13}) results in relatively informative images from which we conclude that the data using a 1-GHz bandwidth noiselet signal can also preserve valuable information about the target.

7. CONCLUSIONS

This paper introduces the concept and applications of noiselet waveforms for multiresolution imaging of various types of defected multilayered structures. The imaging algorithm is developed and tested for imaging of several structural types at different resolutions, high to low. The performance of the noiselet waveform is compared with a traditional wavelet waveform, namely, the Mexican Hat wavelet. It is found that the noiselet better preserves the structural correlations compared to the wavelet, thereby suggesting its advantage over the wavelet for multiresolution analysis. In addition, a modified image difference algorithm developed by us shows promise in exploting the multiresolution images for characterizing the internal features of multilayered structures.

ACKNOWLEDGMENT

This work was supported by the US Office of Naval Research Contract Number N00014-15-1-2021 (POC: William Nickerson).

REFERENCES

1. Coifman, R., F. Geshwind, and Y. Meyer, "Noiselets," *Appl. Comput. Harmon. Anal.*, Vol. 10, No. 1, 27–44, 2001.
2. Candes, E. and J. Romberg, "Sparsity and incoherence in compressive sampling," *Inverse Prob.*, Vol. 23, 969–985, 2007.
3. Keep, D. N., "Frequency-modulation radar for use in the mercantile marine," *Proc. IEE — Part B: Radio Electr. Electron.*, Vol. 103, No. 10, 519–523, 1956.
4. Narayanan, R. M., "Through-wall radar imaging using UWB noise waveforms," *J. Franklin Inst.*, Vol. 345, No. 6, 659–678, 2008.
5. Ferguson, B., S. Mosel, W. Brodie-Tyrrell, M. Trinkle, and D. Gray, "Characterisation of an L-band digital noise radar," *Proc. 2007 IET International Conf. on Radar Systems*, Edinburgh, UK, Oct. 2007, doi: 10.1049/cp:20070634.
6. Axelsson, S. R., "Noise radar using random phase and frequency modulation," *IEEE Trans. on Geoscience and Remote Sensing*, Vol. 42, No. 11, 2370–2384, 2004.
7. Foucher, S., G. B. Benie, and J. M. Boucher, "Multiscale MAP filtering of SAR images," *IEEE Trans. Image Process.*, Vol. 10, No. 1, 49–60, 2001.
8. Graps, A., "An introduction to wavelets," *IEEE Comput. Sci. Eng.*, Vol. 2, No. 2, 50–61, 1995.
9. Peng, Z. K. and F. L. Chu, "Application of the wavelet transform in machine condition monitoring and fault diagnostics: A review with bibliography," *Mech. Syst. Sig. Process.*, Vol. 18, No. 2, 199–221, 2004.

10. Walnut, D. F., *An Introduction to Wavelet Analysis*, Springer Science & Business Media, New York, NY, USA, 2014.
11. Akansu, A. N. and R. A. Haddad, *Multiresolution Signal Decomposition: Transforms, Subbands, and Wavelets*, Academic Press, San Diego, CA, USA, 2001.
12. Rajaraman, P., N. A. Sundaravaradan, R. Meyur, M. J. B. Reddy, and D. K. Mohanta, "Fault classification in transmission lines using wavelet multiresolution analysis," *IEEE Potentials*, Vol. 35, No. 1, 38–44, 2016.
13. Rohwer, C., "Multiresolution analysis of sequences," *Nonlinear Smoothing and Multiresolution Analysis*, Chapter 7, 71–90, Birkhäuser Verlag, Basel, Switzerland, 2005.
14. Sadiku, M. N. O., C. Akujuobi, and R. C. Garcia, "An introduction to wavelets in electromagnetics," *IEEE Microwave Mag.*, Vol. 6, No. 2, 63–72, 2005.
15. Wang, N., Y. Zhang, and S. Wu, "Radar waveform design and target detection using wavelets," *Proc. 2001 CIE International Conf. on Radar*, 506–509, Beijing, China, Oct. 2001.
16. Peele, L. C. and A. N. Pergande, "Wavelet-based radar," United States Patent No. 5,990,823, 23, Nov. 1999.
17. Wang, L., S. Law, C. Fraker, R. Vela, Y. F. Zheng, R. Ewing, and G. Scalzi, "Development of a new software-defined S-band radar and its use in the test of wavelet-based waveforms," *Proc. 2011 IEEE National Aerospace and Electronics Conf. (NAECON)*, 162–166, Fairborn, OH, USA, Jul. 2011.
18. Cao, S., Y. F. Zheng, and R. L. Ewing, "Wavelet-based radar waveform adaptable for different operation conditions," *Proc. 10th European Radar Conf.*, 149–152, Nuremberg, Germany, Oct. 2013.
19. Cao, S., Y. F. Zheng, and R. L. Ewing, "Wavelet-based waveform for effective sidelobe suppression in radar signal," *IEEE Trans. Aerosp. Electron. Syst.*, Vol. 50, No. 1, 265–284, 2014.
20. Cao, S., Y. F. Zheng, and R. L. Ewing, "Wavelet-based radar waveform for moving targets detection," *Proc. 2014 IEEE Radar Conf.*, 1149–1154, Cincinnati, OH, USA, May 2014.
21. Cao, S., Y. F. Zheng, and R. L. Ewing, "Wavelet-based Gaussian waveform for spotlight synthetic aperture radar," *Proc. 2014 IEEE National Aerospace and Electronics Conf. (NAECON)*, 267–273, Dayton, OH, USA, Jun. 2014.
22. Cao, S., Y. F. Zheng, and R. L. Ewing, "A wavelet-packet-based radar waveform for high resolution in range and velocity detection," *IEEE Trans. Geosci. Remote Sens.*, Vol. 53, No. 1, 229–243, 2015.
23. Sullivan, E. J., R. P. Goddard, H. A. Greenbaum, and K. P. Bongiovanni, "Generating simulated reverberation using noiselets," *J. Acoust. Soc. Am.*, Vol. 119, No. 5, Pt. 2, 3273, 2006.
24. Matsumoto, M. and N. Takuji, "Mersenne twister: A 623-dimensionally equidistributed uniform pseudo-random number generator," *ACM Trans. Model. Comput. Simul. (TOMACS)*, Vol. 8, No. 1, 3–30, 1998.
25. Balanis, C. A., *Advanced Engineering Electromagnetics*, John Wiley & Sons, New York, NY, USA, 1999.
26. Richards, M. A., *Fundamentals of Radar Signal Processing*, McGraw-Hill, New York, NY, USA, 2005.
27. Martinez-Lorenzo, J. A., F. Quivira, and C. M. Rappaport, "SAR imaging of suicide bombers wearing concealed explosive threats," *Progress In Electromagnetics Research*, Vol. 125, 255–272, 2012.
28. Dehmollaian, M., and K. Sarabandi, "Refocusing through building walls using synthetic aperture radar," *IEEE Trans. Geosci. Remote Sens.*, Vol. 46, No. 6, 1589–1599, 2008.
29. Stolt, R. H., "Migration by Fourier transform," *Geophys.*, Vol. 43, No. 1, 23–48, 1978.
30. Lopez-Sanchez, J. M. and J. Fortuny-Guasch, "3-D radar imaging using range migration techniques," *IEEE Trans. Antennas Propag.*, Vol. 48, No. 5, 728–737, 2000.
31. Gharamohammadi, A., Y. Norouzi, and H. Aghaeinia, "Optimized UWB signal to shallow buried object imaging," *Progress In Electromagnetics Research Letters*, Vol. 72, 7–10, 2018.